Crystallochemistry and electrical properties of Al-doped Sr_2SiO_4 electrolytes

Porras-Vazquez, JM; dos Santos-Gómez, L. ; Slater, Peter; Marrero-López, D. ; Losilla, E.R.

DOI:
10.1016/j.ceramint.2016.07.183

Document Version
Peer reviewed version

Citation for published version (Harvard):
Porras-Vazquez, JM, dos Santos-Gómez, L, Slater, P, Marrero-López, D & Losilla, ER 2016, 'Crystallochemistry and electrical properties of Al-doped Sr_2SiO_4 electrolytes', *Ceramics International*, vol. 42, no. 14, pp. 16317-16324. https://doi.org/10.1016/j.ceramint.2016.07.183

Crystallochemistryand electrical properties of Al-doped Sr_2SiO_4 electrolytes

J.M. Porras-Vázquez, L. dos Santos-Gómez, P.R. Slater, D. Marrero-López, E.R. Losilla

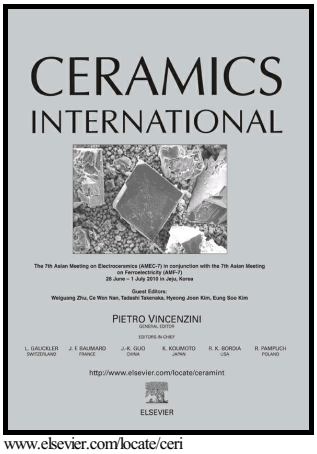

www.elsevier.com/locate/ceri

PII: S0272-8842(16)31259-7
DOI: http://dx.doi.org/10.1016/j.ceramint.2016.07.183
Reference: CERI13408

To appear in: *Ceramics International*

Received date: 29 June 2016
Revised date: 25 July 2016
Accepted date: 26 July 2016

Cite this article as: J.M. Porras-Vázquez, L. dos Santos-Gómez, P.R. Slater, D Marrero-López and E.R. Losilla, Crystallochemistryand electrical properties o Al-doped Sr_2SiO_4 electrolytes, *Ceramics Internationa* http://dx.doi.org/10.1016/j.ceramint.2016.07.183

Crystallochemistry and electrical properties of Al-doped Sr_2SiO_4 electrolytes

J.M. Porras-Vázquez[1,*], L. dos Santos-Gómez[1], P.R. Slater[2], D. Marrero-López[3], E. R. Losilla[1]

[1] *Universidad de Málaga, Dpto. de Química Inorgánica, 29071-Málaga, Spain.*

[2]*School of Chemistry, University of Birmingham, Birmingham, B15 2TT, UK*

[3] *Universidad de Málaga, Dpto. de Física Aplicada I, Laboratorio de Materiales y Superficies (Unidad Asociada al C.S.I.C.), 29071-Málaga, Spain.*

Abstract

A new $Sr_2Si_{1-x}Al_xO_{4-x/2}\square_{x/2}$ (x=0, 0.028, 0.06 and 0.075) silicate series has been prepared and the structural and electrical properties were investigated. These samples present three different polymorphs (β, α'_L and α'_H) and the increase of Al-content resulted in a shift of the polymorph content, from a monoclinic form to an orthorhombic one. Aluminium contents higher than x = 0.06 did not lead to any further change in the ratio of polymorphs. High temperature X-ray diffraction studies showed a complete stabilization of α'_L, presenting a superstructure orthorhombic form, at temperatures between RT and 250 ºC. At temperatures higher than 500 ºC a basic orthorhombic cell is stabilised. Thermogravimetric analysis displayed an increase of the water uptake on doping, due to the generation of oxide vacancies in the lattice. Electrical characterization in dry and wet atmospheres showed an important proton contribution to the conductivity. In addition, measurements in N_2 and O_2 fluxes displayed a significant p-type electronic contribution to the overall conductivity.

Keywords: SOFC, electrolyte, Sr_2SiO_4, Al-doping

* Corresponding author.

E-mail address: josema@uma.es (José Manuel Porras Vázquez)

Present address: Dpto. de Química Inorgánica, Facultad de Ciencias, Campus de Teatinos, Universidad de Málaga, 29071-Málaga, Spain.

Tel: +34 952132022, Fax: +34 952131870

1. Introduction

Ceramic ion conductors have numerous applications in different areas, such as sensors, fuel cells, etc. Yttria stabilized zirconia (YSZ) [1] and gadolinia doped ceria (CGO) [2], with a fluorite structure, are the state-of-the art materials. However, these materials present several inconveniences, such as a necessity for high operation temperatures and low stability in reducing environments, respectively. Alternative oxide ion conductors with different structures have also been investigated: materials based on a perovskite, such as $La_{0.9}Sr_{0.1}Ga_{0.8}Mg_{0.2}O_{2.85}\square_{0.15}$ [3]; brownmillerite-type, such as $Ba_2In_2O_5$ [4]; $La_2Mo_2O_9$ [5]; apatite-based structure, such as $La_{9.33}Si_6O_{26}$ [6]; $LaBaGaO_4$-like, with β-K_2SO_4 type structure [7]; and, melilite-type, such as $LaSrGa_3O_7$ [8].

Proton conductors have received great attention due to their generally better conductivity at reduced operation temperatures. Most of the research on electrolytes for proton conductors solid oxide fuel cells (PC-SOFCs) has been focused on perovskite-type materials based on $BaCeO_3$ and $BaZrO_3$ [9-12]. The former are the state-of-the-art, with very high conductivity values (~10^{-2} S cm^{-1} at 600 ºC), however, these materials are prone to carbonation in the presence of CO_2. [13,14] For the latter, $BaZrO_3$ has a much better chemical stability towards CO_2, however, the high temperatures required for the preparation of dense ceramics lead to high grain boundary resistances and low conductivity values.

In the last few years, our research group have been involved in the identification of new electrolytes for intermediate temperature SOFCs, mainly focusing on systems where "loosely bound" oxide anions were the charge carriers, for instance, $Ca_3(SiO_4)O$ [15,16], $Sr_3(SiO_4)O$ [17] and $Ln_2(TO_4)O$ (Ln=La, Nd, T= Si, Ge) [18]. In those systems four oxygen atoms form part of isolated tetrahedral units and the remaining one is "loosely bound" and prone to present a higher mobility. In order to enhance the conductivity, different doping strategies in the tetrahedral position were carried out to increase the

oxygen vacancy concentration. As result, moderate conductivity values (~10^{-4} S cm^{-1} at 800 ºC) were observed, with the presence of a significant proton contribution to the overall conductivity.

Very recently, the structural and electrical properties of aluminium doped dicalcium silicate, Ca_2SiO_4, a major constituent of belite Portland cements, were studied. [19] Dicalcium silicate exhibits several polymorphs on heating (γ, β, α'_L, α'_H and α) and it is worth mentioning that the transition β (monoclinic) → γ (orthorhombic) gives rise to a significant change in the cell volume, degrading the material. [20-22] Cuesta *et al.* [19] demonstrated that Al-doping in the silicon position stabilized the β form, preventing the formation of the γ-polymorph and the consequent ceramic failure. In addition, an increase in conductivity was observed on doping, due to the generation of oxide vacancies.

The analogous distrontium silicate exhibits three polymorphs: a monoclinic form similar to β-Ca_2SiO_4, and two orthorhombic polymorphs on heating, the first one displaying a superstructure cell, both related to α'_L and α'_H-Ca_2SiO_4, respectively. [23-31] The structure of Sr_2SiO_4 is analogous to that of Ca_2SiO_4 and based on similar structural units: M^{2+} ions (M = Ca, Sr) and isolated SiO_4 tetrahedra, where there are two different strontium sites, Sr1 and Sr2, seven- and eight-fold coordinated, respectively. The structure of both monoclinic and orthorhombic Sr_2SiO_4 polymorph are displayed in Fig. 1.

Adopting the nomenclature used for Ca_2SiO_4, it is worth mentioning that the transitions β → α'_L and α'_L → α'_H occur at ~85 and ~500 ºC, respectively, much lower temperatures than for Ca_2SiO_4, where the analogous transitions take place at 690 and 1160 ºC, respectively. [30] The α′ form of Sr_2SiO_4 is expected to be stabilized at room temperature by doping with appropriate cations. In addition, it has been reported that the α′ form of Sr_2SiO_4 may be stabilized at room temperature through replacing Sr by small amounts of Ba. [25]

The objective of the present study is to investigate the effect of Al-doping on the structure and electrical properties of Sr_2SiO_4-based materials. An enhancement in the electrical properties is expected

due to the fact that the aliovalent substitution of silicon by aluminium generates oxide vacancies in the lattice.

2. Experimental section

2.1 Synthesis and powder characterization

$Sr_2Si_{1-x}Al_xO_{4-x/2}\square_{x/2}$ (x= 0, 0.028, 0.06 and 0.075) series was synthesized by reactive sintering using high-purity oxides and carbonates as starting materials: $SrCO_3$ (Alfa, 99.99%), SiO_2 (Alfa, 99.5%) and γ-Al_2O_3 (Alfa, 99.997%). Strontium carbonate was precalcined at 1400 ºC for 15 h in order to achieve its full decarbonation. Raw mixtures were ground and preheated at 1050 ºC for 4 hours (heating rate of 10 ºC min^{-1}) in order to prepare 3 g of each sample. Under these conditions only a partial reaction takes place. The resulting powders were reground in a Fritsch ball mill (model Pulverisette 7, 45 cm^3 agate vessel containing 7 agate balls with a diameter of 15 mm) for 30 min at 200 rpm with reverse rotation every 10 min and pelletized (10 mm diameter, ~1 mm of thickness, 500 MPa). A second thermal treatment was carried out at 1550 ºC for 6 hours (heating rate of 10 ºC min^{-1}) and the sample was slowly cooled down to room temperature (10 ºC min^{-1}). Compaction was calculated taking into account the pellet mass, volume and the crystallographic density. Three pellets were prepared under identical experimental conditions: one (after grinding) for the structural and thermal analysis and two additional ones for impedance and microstructural characterization, respectively. Hereafter, $Sr_2Si_{1-x}Al_xO_{4-x/2}\square_{x/2}$ series is labelled as Sr_2Al_x (Table 1).

X-ray powder diffraction (XRPD) patterns were recorded using a PANalytical X´Pert Pro diffractometer with $CuK_{\alpha 1}$ radiation to determine the purity and polymorphism of the materials. Variable temperature experiments were carried out in an Anton Paar HTK1200 under static air. Data were collected at 30, 250, 500, 750 and 900 ºC after a delay time of 15 min at each temperature to ensure thermal stabilization.

Phase identification was performed with X´Pert HighScore Plus [32] and Rietveld analysis with GSAS software [33] using the ICSD database for the starting structural models [34]. The usual profile parameters (scale factors, background coefficients, zero-points, half-width, pseudo-Voigt

and asymmetry parameters for the peak-shape) were refined. The atomic parameters were fixed and not refined.

2.2. Thermal analysis

Thermogravimetric analysis (TGA) data were recorded on a SDT-Q600 analyzer supplied by TA Instruments. The temperature was varied from RT to 900 ºC at a heating/cooling rate of 10 ºC min^{-1}. Different heating/cooling cycles were carried out to study the thermal reversibility and reproducibility of the measurements on samples in open platinum crucibles under a mixed flow of dry-air (10 mL min^{-1}) and wet-air (15 mL min^{-1}) saturated by bubbling in water at 20 ºC.

2.3. Microstructural characterization and conductivity measurements

The microstructure of the ceramics was observed by scanning electron microscopy (SEM) (Jeol JSM-6490LV) combined with energy dispersive spectroscopy (EDS). The grain size of the sintered pellets was estimated from SEM micrographs, using the linear intercept method from at least 30 random lines and three different micrographs with the help of image-analysis software. [35] Platinum electrodes were made by coating opposite pellet faces with METALOR® 6082 platinum ink and heating to 800 ºC at a rate of 5 ºC min^{-1} for 15 min in air to decompose the paste and to harden the Pt residue. Impedance spectra were obtained using a frequency response analyser (Solartron 1260) in different dry and wet gases (N_2 and O_2) in the 0.1 Hz to 1 MHz frequency range with an ac perturbation of 100 mV. The spectra were recorded upon cooling from 900 to 500 ºC with a stabilization time of 10 minutes between consecutive measurements. Impedance spectra were analyzed using the ZView program. [36] The resistance and capacitance values of the different contributions were obtained by fitting the impedance spectra data with an equivalent circuits formed by (RQ) elements in series, where R is a resistance and Q is a pseudocapacitance in parallel.

Conductivity measurements as a function of oxygen partial pressure $p(O_2)$, from $\sim 10^{-22}$ atm to 0.21 atm were performed in a closed tube-furnace cell. $p(O_2)$ values were monitored using a YSZ oxygen sensor positioned close to the sample. The conductivity was continuously recorded as a function of $p(O_2)$. The process consisted of flushing the system with a dry gas mixture of 5% H_2 in

Ar for 12 h at 800 ºC and 900 ºC in order to reach a minimum in oxygen activity inside the furnace and ensure that the sample was close to the equilibrium under those conditions. Next, the flushing was switched off, and the oxygen partial pressure was allowed to slowly recover to atmospheric pressure by free diffusion, since the system was not fully airtight. Each isothermal cycle took more than 48 h to complete.

The ion transference numbers were determined by the modified electromotive force method (emf) proposed by Gorelov. [37,38] This modification of the classical emf technique eliminates possible errors in the determination of ion transference numbers, arising due to electrode polarization. These errors are not negligible for electrolyte materials which have relatively low electronic conductivity. [38,39] The ionic transport numbers, t_o, were measured under a $p(O_2)$ gradient of dry 5%H_2–Ar/air, using a continuous flux of these gases in the 650-900 ºC temperature range. A YSZ tube was used to measure the theoretical emf under these conditions, E_{th}. The emf observed in the sample, E_{obs}, was measured with an external variable resistance R_M, in parallel to the measuring cell, varying from 100 MΩ to 1.5 kΩ. Experimental data were fitted with the equivalent circuit (Eqn (1)) proposed by Gorelov. [37,40] In this case, the ionic resistance R_o, the electronic resistance R_e and the polarization resistance R_η are related to the emf values (E_{th} and E_{obs}) from the relationship:

$$\frac{E_{th}}{E_{obs}} - 1 = (R_O + R_\eta)\left[\frac{1}{R_e} + \frac{1}{R_M}\right] \quad (1)$$

The dependence of $(E_{th}/E_{obs} - 1)$ vs $1/R_M$ is a linear plot with slope $(R_o + R_\eta)$ and the intercept of the $(1/R_M)$-axis is equal to $(-1/R_e)$. Total resistance R_T was determined independently by impedance spectra data. Oxide ion transport numbers were calculated as: $t_o = 1 - R_T/R_e$.

3. Results and discussion

3.1. Single phase existence ranges

The samples were prepared by reactive sintering, a method where the synthesis and densification process take place in a single heating step. This methodology have been proven useful

with different materials, leading to pure and dense ceramic samples with an adequate microstructure [19,41]. After the heating process the pellet samples were ground and studied by X-ray powder diffraction.

XRPD patterns for $Sr_2Si_{1-x}Al_xO_{4-x/2}\square_{x/2}$ (x= 0, 0.028, 0.06 and 0.075) series are shown in Fig. 2. All samples are composed by two related polymorphs without the presence of any additional secondary phases. The solubility limit of aluminium in the reactive sintering conditions at 1550 ºC is close to x=0.06, above this concentration the cell volumes are quite similar, indicating that more aluminium cannot be incorporated into the structure. (see Table 1).

Rietveld refinements were performed by fitting only the overall parameters and weight fractions for all the phases. For the monoclinic phase, the structural description, previously reported by Catti *et al.,* was used [25]. For the orthorhombic structure, the models available in the ICSD database (No. 35666 and 35667), claimed to represent Sr_2SiO_4 above 85ºC, did not satisfactory fit the XRPD pattern, where some small reflections were not given any intensity. [25,30]. However, as was reported by Withers *et al.* [30] and Liu *et al.* [31], the polymorph above 85 ºC presents a tripled superstructure, therefore, a structural model from the analogous α'_L-Ca_2SiO_4 was used, where the a-axis is multiplied by three. Ca atoms were replaced by Sr and cell parameters where appropriately modified to match the basic unit cell for this polymorph. With this phase all small reflections were satisfactory fitted.

Fig. 3 shows an example of the fit for $Sr_2Al_{0.06}$. Good agreements factors were achieved (Table 1). The undoped phase, Sr_2SiO_4, shows at room temperature two different polymorphs, monoclinic (β) and orthorhombic (α'_L), with percentages of 88 and 12 wt.%, respectively (Table 1). However, as the aluminium content increases the orthorhombic phase turns to be the main phase, with values close to 92 wt.%. For Al content x >0.06 no change in the polymorph ratio is observed. It has to be noted that Al-doped Sr_2SiO_4 series present a different behaviour to analogous Ca_2SiO_4 [19]. The undoped calcium sample shows a mixture of β monoclinic and γ orthorhombic

polymorphs at room temperature, with the % monoclinic form increasing on Al-doping, with a 99 and 1 wt.% of β and γ–Ca_2SiO_4, respectively, for $Ca_2Al_{0.028}$.

As can be seen in Table 1, the unit cell parameters and cell volumes for $Sr_2Si_{1-x}Al_xO_{4-x/2}\square_{x/2}$ increase on doping, reaching its maximum at x=0.06, indicating the end of the successful replacement of Si by Al. This behaviour is expected due to the fact that Al^{3+} (0.39 Å) has a larger ionic radius than Si^{4+} (0.26 Å) in a tetrahedral environment. This result further confirms the partial substitution of silicon by aluminium.

XRPD experiments on heating for $Sr_2Al_{0.06}$ showed a transition between RT and 250 ºC from a mixture of monoclinic and orthorhombic phases to a fully orthorhombic $Pna2_1$ phase (α'_L). Fig. 4 left and Table 2 show the 25-29 º2θ range, where the reflection assigned to the monoclinic phase (112) disappear. Between 250 and 500 ºC the (002) reflection is no longer present (see Fig. 4 right for the 29-32 º2θ range) where a second polymorphic change was observed, from a superstructure cell to a basic orthorhombic symmetry. In the literature this high temperature orthorhombic phase was reported to be Pmnb, however in this work a Pnma space group, analogous to α'_H-Ca_2SiO_4, was also tested. The latter gave significantly lower R_F values, an improvement of almost 1.5%, thus, Pnma was used in all high temperature refinements. No transition to a hexagonal polymorph, $\alpha'_H \rightarrow \alpha$, as in Ca_2SiO_4, was detected up to 900 ºC. It is worth mentioning that Al doping changes the polymorphism at room temperature but no differences were observed on heating.

The synthesis of $Sr_{2-x/2}Al_{x/2}Si_{1-x/2}Al_{x/2}O_4$ (x= 0.06), where Al is replacing both Sr and Si sites, was also attempted. However, despite the lack of any major segregation of secondary phases, the amount of monoclinic is very high and close to the value for the undoped sample, indicating that Al is not substituting for Sr. A similar behaviour was observed in previous related work for Sr_3SiO_5-based compounds, where Al is only incorporated in Si-site. [17]

3.2. Thermogravimetric analysis

Thermogravimetric measurements were carried out to analyse the effect of aluminium substitution on the oxygen vacancy concentration and water uptake. Measurements were recorded in humidified air and the curves on heating and cooling were completely reproducible. Only the curves acquired on cooling are plotted for better comparison of the data.

As can be seen in Fig. 5, the weight increase on cooling (below 700 ºC) on Al-doping due to the higher oxygen vacancy concentration and the consequent incorporation of water with the formation of protonics defects, taking place as follows (Eq. 2), using the Kröger-Vink notation:

$$\mathbf{H_2O(g) + O_O^x + v_O^{\bullet\bullet} \rightarrow 2OH_O^{\bullet}} \quad (2)$$

This water uptake is clearly seen if the mass gain for the undoped composition, Sr_2Al_0, 0.01 wt% (0.001 moles of water per unit formula), is compared to that for $Sr_2Al_{0.075}$, 0.07% (0.010 moles of water per unit formula). For $Sr_2Al_{0.075}$ in dry conditions, the water uptake is significantly lower, 0.01 wt% (0.001 moles of water per unit formula), due to the no incorporation of water into the vacancies.

In the very high temperature region, 700-900 ºC, a minor weight change is also observed likely ascribed to the oxygen uptake/desorption into the vacancies of the structure. This phenomenon will be further studied by impedance spectroscopy in the next section.

3.3. Microstructural analysis

The sintering conditions led to dense samples with compactions increasing on doping, for instance, $Sr_2Al_{0.0}$ exhibits a relative density of 85% and this value increases up to 95% for the Al-doped compounds. Fig. 6 shows the SEM micrographs of the sintered pellets, which show that the average grain size grows with the Al-doping: 3.6, 5.3, 6.3 and 8.5 μm for $Sr_2Al_{0.0}$, $Sr_2Al_{0.028}$, $Sr_2Al_{0.06}$ and $Sr_2Al_{0.075}$, respectively. Regarding porosity, it is significantly high for the undoped composition, as is reflected by the moderate compaction value about 85%. For the Al-doped samples the porosity decreases dramatically, indicating clearly that Al-doping improve the

densification and grain growth rate. No indications of liquid phase formation or phase segregations are found at the grain boundary region. Additionally, no contamination due to the ball-milling process was detected in the sintered pellets.

3.4. Electrochemical characterization

Impedance spectroscopy was carried out to analyse the electrical properties of the samples and establish the existence of mixed ionic oxide-proton conductivity. For this purpose, the measurements were performed under different flowing gases: dry and wet N_2 and O_2 gases. Fig. 7 shows representative impedance plots for $Sr_2Al_{0.06}$ measured in the different gases at 800 ºC. It is clear that there is only one contribution to the conductivity, ascribed to the grain interior with capacitance values of 4.7 pF cm^{-1}. Note that the grain boundary contribution is negligible in these samples. In addition, the impedance data were very well fitted to the following equivalent circuit: $(R_bQ_b)Q_e$, using the Zview program [36], where the subscripts b and e denote grain interior (bulk) and electrode processes, respectively.

Fig. 8 shows the Arrhenius plots of the overall conductivity for Sr_2Al_0 and $Sr_2Al_{0.06}$ samples under different atmospheres. It is quite evident from these impedance spectroscopy measurements that these materials present a significant proton contribution to the overall conductivity, with conductivities always higher in wet atmospheres in the whole temperature range studied, indicating that a minor fraction of water is retained in the structure even at high temperature, which is supported by the thermogravimetric analysis.

It is also very clear that there is an increase of the conductivity on doping, for instance, the total conductivity values in wet N_2 for Sr_2Al_0 and $Sr_2Al_{0.06}$ at 800 ºC are 4.3 10^{-6} and 2.5 10^{-5} S cm^{-1}, respectively, a clear indication of the generation of oxide vacancies derived from the substitution of Si^{4+} by Al^{3+} (see Table 3). It should also be commented that the conductivity of these samples is higher than those reported for analogous Ca_2SiO_4 [19]. For instance, the conductivity of $Ca_2Al_{0.028}$ were 2.7 10^{-5} and 2.5 10^{-6} S cm^{-1} in wet O_2 and dry N_2, respectively, at 900 ºC, and the values for $Sr_2Al_{0.028}$ were 5.5 10^{-5} and 1.7 10^{-5} S cm^{-1}, respectively, in the same conditions. In addition, all the

samples measured in dry atmospheres present activation energies ranging between 1.2 and 1.3 eV, typical values for oxide ion conductivity. In the case of wet atmospheres the activation energy decreases to values ranging between 1.0 and 1.1 eV, as expected when a proton is implicated in the conductivity with better mobility and consequently lower activation energy.

The increase in the conductivity on Al doping can be correlated with the increase in the O vacancy concentration, which will lead to an increase in the oxide ion conductivity, along with a protonic contribution to the conductivity in wet atmospheres due to water incorporation into these oxide ion vacancies (Eq. 2). An interesting feature to consider is how these oxide ion vacancies are accommodated in the structure. Since Si is tetrahedral, the introduction of O vacancies on Al doping might at first glance be expected to give some 3 coordinate Si or Al. Such a low coordination situation might, however, be expected to be unfavourable, and rather we can propose that the O vacancies are accommodated by condensation with adjacent Si/AlO_4 units. Thus O vacancies could be accommodated by the formation of either $(Si/Al)_2O_7$ or $(Si/Al)_3O_{11}$ similar to the types of defects proposed for related $La_{1-x}Ba_{1+x}GaO_{4-x/2}$ and $La_{1-x}Ca_xNbO_{4-x/2}$ [7,43]. In this way the O vacancy defect is accommodated in the structure while maintaining the tetrahedral coordination. In terms of oxide ion migration, prior modelling studies of structurally related $La_{1-x}Ba_{1+x}GaO_{4-x/2}$ suggested a conduction mechanism via a cooperative "cog-wheel –type" process involving the breaking and reforming of these units [7], and a similar mechanism is likely here. In order to confirm this mechanism, $Sr_{1.94}La_{0.06}SiO_{4.03}$, a composition without oxygen vacancies was prepared. For that sample it was observed a significant drop in the conductivity, 1.1 10^{-7} S cm^{-1} at 800 ºC, and an important increase in the activation energy, 1.90 eV (see Fig. 8), due to the absence of oxygen vacancies and the no possibility of a "cog-wheel type" conduction mechanism.

In terms of proton conduction, the water incorporation would lead to the break up of these units to give $(Si/Al)O_4H$ units. Proton migration would then be a combination of proton migration around the tetrahedral unit (intra-tetrahedron motion) and between adjacent tetrahedral units (inter-tetrahedron motion). Further computer modelling studies would be required to elucidate whether, as

for $La_{1-x}Ba_{1+x}GaO_{4-x/2}$, the former intra-tetrahedron motion is the rate-limiting step for long range proton motion.

It is very important to also note that the conductivities increases under oxidising conditions, likely due to a small p-type electronic contribution to the conductivity, following the next equation, Eqn.3:

$$\frac{1}{2}\mathbf{O_2(g)} + \mathbf{v_O^{\bullet\bullet}} \rightarrow \mathbf{O_O^x} + \mathbf{2h^{\prime}} \quad (3)$$

Increasing the aluminium content increases the amount of holes which leads to higher p-type electronic conductivity on Al doping. This behaviour was already observed for Ca_2SiO_4 and M_3SiO_5-based (M= Ca and Sr) materials, which also exhibit a p-type electronic contribution to the conductivity.

Conductivity measurements in varying oxygen partial pressure were also performed, confirming the presence of a p-type electronic contribution at high $p(O_2)$ values. At intermediate temperatures, a plateau region is observed and ascribed to the pure ion conduction (proton and oxide). Finally, at very low $p(O_2)$ values, a very significant decrease in the conductivity is observed. This behaviour has been previously reported in related materials [15-17, 19] and it is ascribed to a drop in the water partial pressure at low $p(O_2)$ values. This results in a sudden decrease of the proton conductivity. It is worth mentioning that at very low oxygen partial pressures, and at 800 ºC, a second plateau is observed, where the only contribution to the overall conductivity is ascribed to oxide species. These results confirmed the behaviour observed in Fig. 8, where the samples still present proton conductivity at high temperature, a trend that was already observed for other electrolytes such as $La_2Zr_2O_7$, $SrZrO_3$, $BaCeO_3$ [44-48].and related $(Ca,Sr)_3SiO_5$ and Ca_2SiO_4-based materials [15-17, 19].

Oxide transference numbers were estimated by a modified electromotive force to take into consideration the electrode polarization of the samples. The measurements were carried out under ambient 5%H_2-Ar/air gradient to confirm that the materials are ionic conductors in these conditions.

The ion transference number decreases from 0.94 to 0.81 in the 900-650 ºC temperature range (Fig.9 inset). This significant lowering in the values can be assigned to a higher contribution of the proton mobility at lower temperatures. As it can be seen in Fig. 8, dry and wet measurements, for both atmospheres, became more comparable as the temperature increases, therefore, the higher proton contribution is reflected on the ion transference number as the temperature decreases. In addition, there is significant electronic p-type contribution to the conductivity that reduces the ion transference numbers at elevated temperatures (see Fig. 8 and 9).

Conclusions

Aluminium is successfully incorporated into the structure of distrontium silicate, leading to the almost complete stabilization of the superstructure orthorhombic polymorph ($Pna2_1$ space group) at room temperature. XRPD experiments on heating showed a full transition from the monoclinic form to the orthorhombic one between RT and 250 ºC. At temperatures beyond 250 ºC it was observed a complete transit to a basic orthorhombic cell (Pnma). Thermogravimetric analysis and impedance spectroscopy confirmed the formation of oxide vacancies on doping due to an increase in the water uptake and the enhancement of the electrical conductivity. Measurements in wet atmospheres revealed the presence of a very significant proton contribution to the conductivity in the whole range of temperature. Electrical conductivity measurements as a function of the oxygen partial pressure displayed proton conductivity and a small p-type electronic contribution at reducing and oxidizing conditions, respectively. However, the reported conductivities are at least two orders of magnitude lower than that of YSZ but there is room for optimisation in this new family of conductors.

Acknowledgements

This work was funded by Spanish MINECO through MAT2013-41836 which is co-funded by FEDER. L. dos Santos-Gómez thanks to the Spanish Ministry of Education, Culture and Sports for her FPU studentship. J. M. Porras-Vázquez thanks Andalucía Tech for the funding.

References

1. N. Q. Minh, Solid oxide fuel cell technology-features and applications, Solid State Ionics 174 (2004) 271-277.

2. S. Torrens, N. M. Sammes, G. A. Tompsett, Characterisation of $(CeO_2)_{0.8}(GdO_{1.5})_{0.2}$ synthesised using various techniques, Solid State Ionics 111 (1998) 9-15.

3. H. Hayashi, H. Inaba, M. Matsuyama, N. G. Lan, M. Dokiya, H. Tagawa, Solid State Ionics 122 (1999) 1-15.

4. J. B. Goodenough, J. E. Ruiz-Diaz, Y. S. Zhen, Oxide-ion conduction in $Ba_2In_2O_5$ and $Ba_3In_2MO_8$ (M=Ce, Hf, or Zr), Solid State Ionics 44 (1990) 21-31.

5. P. Lacorre, F. Goutenoire, O. Bohnke, R. Retoux, Designing fast oxide-ion conductors based on $La_2Mo_2O_9$, Nature 404 (2000) 856-858.

6. J. R. Tolchard, M. S. Islam, P. R. Slater, Defect chemistry and oxygen ion migration in the apatite-type materials $La_{9.33}Si_6O_{26}$ and $La_8Sr_2Si_6O_{26}$, J. Mater. Chem. 13 (2003) 1956-1961.

7. E. Kendrick, J. Kendrick, K. S. Knight, M. S. Islam, P. R. Slater, Cooperative mechanisms of fast-ion conduction in gallium-based oxides with tetrahedral moieties, Nat. Mater. 6 (2007) 871-875.

8. C. I. Thomas, X. Kuang, Z. Deng, H. Niu, J. B. Claridge, M. J. Rosseinsky, Phase stability control of interstitial oxide ion conductivity in the $La_{1+x}Sr_{1-x}Ga_3O_{7+x/2}$ melilite family, Chem Mater. 22 (2010) 2510-2516.

9. H. Iwahara, H. Uchida, K. Ono, K. J. Ogaki, Proton conduction in sintered oxides based on $BaCeO_3$, J. Electrochem. Soc. 135 (1988) 529-533.

10. H. Iwahara, T. Yajima, H. Ushida, Effect of ionic-radii of dopants on mixed ionic-conduction (H^++O^{2-}) in $BaCeO_3$-based electrolytes, Solid State Ionics 70 (1994) 267-271.

11. D. Shima, S. M. Haile, The influence of cation non-stoichiometry on the properties of undoped and gadolinia-doped barium cerate, Solid State Ionics 97 (1997) 443-455.

12. K. Katahira, Y. Kohchi, T. Shimura, H. Iwahara, Protonic conduction in Zr-substituted $BaCeO_3$, Solid State Ionics 138 (2000) 91-98.

13. K. H. Ryu, S. M. Haile, Chemical stability and proton conductivity of doped $BaCeO_3$-$BaZrO_3$ solid solutions, Solid State Ionics 125 (1999) 355-367.

14. N. Zakowsky, S. Williamson, J. T. S. Irvine, Elaboration of CO_2 tolerance limits of $BaCe_{0.9}Y_{0.1}O_3$-delta electrolytes for fuel cells and other applications, Solid State Ionics 176 (2005) 3019-3026.

15. J. M. Porras-Vázquez, A. G. de la Torre, D. Marrero-López, E. R. Losilla, M. A. G. Aranda, A new family of oxide ion conductors based on tricalcium oxy-silicate, Dalton Trans. (2006) 2691-2697.

16. J. M. Porras-Vázquez, A. G. De la Torre, E. R. Losilla, M. A. G. Aranda, Oxide and proton conductivity in aluminum-doped tricalcium oxy-silicate, *Solid State Ionics*, 2007, **178**, 1073.

17. J. M. Porras-Vázquez, E. R. Losilla, L. León-Reina, M. Martínez-Lara, M. A. G. Aranda, Synthesis and characterization of a new family of mixed oxide-proton conductors based on tristrontium oxysilicate, Chem. Mater. 20 (2008) 2026-2034.

18. L. Leon-Reina, J. M. Porras-Vazquez, E. R. Losilla, L. Moreno-Real, M. A. G. Aranda, Structure and oxide anion conductivity in $Ln_2(TO_4)O$ (Ln = La, Nd; T = Ge, Si), J Solid State Chem. 181 (2008) 2501-2056.

19. A. Cuesta, M. A. G. Aranda, J. Sanz, A. G. de la Torre, E. R. Losilla, Mechanism of stabilization of dicalcium silicate solid solution with aluminium, Dalton Trans. 43 (2014) 2176-2182.

20. S. N. Ghosh, P. B. Rao, A. K. Paul, K. J. Raina, Chemistry of dicalcium silicate mineral, J. Mater. Sci. 14 (1979) 1554-1566.

21. M. Regourd, M. Bigare, J. Forest, A. Guinier, Proceedings of the 5th International Symposium on the Chemistry of Cement, Part I, Supplement Paper I-10, Tokyo, 1968, 44.

22. C. M. Midgley, The crystal structure of beta-dicalcium silicate, Acta Crystallogr. 5 (1952) 307-312.

23. H. O'Damel, L. Tscheischwili, On the structure of K_2BeF_4, Sr_2SiO_4 and Ba_2SiO_4, Z. Kristallogr. 104 (1942) 348-357.

24. G. Pieper, W. Eysel, T. H. Hahn, Solid solubility and polymorphism in system Sr_2SiO_4-Sr_2GeO_4-Ba_2GeO_4-Ba_2SiO_4, J. Am. Ceram. Soc. 55 (1972) 619-622.

25. M. Catti, G. Gazzoni, G. Ivaldi, Structures of twinned beta-Sr_2SiO_4 and of alpha'-$Sr_{1.9}Ba_{0.1}SiO_4$ Acta Cryst. C39 (1983) 29-34.

26. M. Catti, G. Gazzoni, G. Ivaldi and G. Zanini, The beta-reversible-alpha'-phase transition of Sr_2SiO_4.1. Order-disorder in the structure of the alpha'-form at 383K, Acta Cryst. B39 (1983) 674-679.

27. R. Heindl, A. Amara, G. Tary, J. Loriers, On the polymorphism of Sr_2SiO_4 - a high-pressure monoclinic phase and an orthorhombic phase, J. Mater. Sci. Lett. 4 (1985) 1449-1450.

28. L. Stenberg, B. G. Hyde, A preliminary electron-microscope study of the beta-reversible-alpha' transformation of distrontium silicate, Sr_2SiO_4, Acta Cryst. B42 (1986) 417-422.

29. B. G. Hyde, J. R. Sellar, L. Stenberg, The beta-reversible-alpha' transition in Sr_2SiO_4 (and Ca_2SiO_4, K_2SeO_4 etc), involving a modulated structure, Acta Cryst. B42 (1986) 423-429.

30. R. L. Withers, B. G. Hyde, J. G. Thompson, An electron-diffraction study of the incommensurately modulated alpha'-L-phase of distrontium silicate, Sr_2SiO_4, J. Phys. C: Solid State Phys. 20 (1987) 1653-1669.

31. J. Liu, C-G. Duan, W. N. Mei, R. W. Smith, J. R. Hardy, Polymorphous transformations in alkaline-earth silicates, J. Chem. Phys. 116 (2002) 3864-3869.

32. X´Pert HighScore Plus Program, Version 3.0e, PANalytical B.V., Amelo, The Netherlands, 2012.

33. A. C. Larson, R. B. von Dreele, GSAS Program, Los Alamos National Lab, 1994. Rep. No. LA-UR-86748.

34. Inorganic Crystal Structure Database, ICSD, 2014, pp. v2014-01.

35. Estereologia, Joao Abrantes, 1998, UIDM, ESTG, Polytechnic Institute of Viana do Castelo, Viana do Castelo, Portugal

36. D. Johnson, ZView: A software program for IES Analysis, Version 2.8, Scribner Associates, Inc., Southern Pines, NC, 2002.

37. V. P. Gorelov, Transport number determinations in ionic conductors using emf-measurements with active load, Sov. Electrochem+. 24 (1988) 1272-1274.

38. I. P. Marozau, D. Marrero-López, A. L. Shaula, V. V. Kharton, E. Tsipis, P. Núñez, J. Frade, Ionic and electronic transport in stabilized beta-$La_2Mo_2O_9$ electrolytes, Electrochim. Acta 49 (2004) 3517-3524.

39. V. V. Kharton, A. P. Viskup, F. M. Figueiredo, E. N. Naumovich, A. A. Yaremchenko, F. M. B. Marques, Electron-hole conduction in Pr-doped Ce(Gd)O_2-delta by faradaic efficiency and emf measurements, Electrochim. Acta 46 (2001) 2879-2889.

40. D. Marrero-López, J. Peña-Martínez, D. Pérez-Coll, P. Núñez, Effects of preparation method on the microstructure and transport properties of $La_2Mo_2O_9$ based materials, J. Alloy. Compd. 422 (2006) 249-257.

41. J. M. Porras-Vázquez, E. R. Losilla, L. León-Reina, D. Marrero-López, M. A. G. Aranda, Microstructure and oxide ion conductivity in a dense $La_{9.33}(SiO_4)_6O_2$ oxy-apatite J. Am. Ceram. Soc. 92 (2009) 1062-1068.

42. K. Amezawa, H. Maekawa, Y. Tomii, N. Yamamoto, Protonic conduction and defect structures in Sr-doped $LaPO_4$, Solid State Ionics 145 (2001) 233-240.

43. R. Hausgrud, T. Norby, Proton conduction in rare-earth ortho-niobates and ortho-tantalates, Nature Materials 5 (2006) 193-196.

44. J. A. Labrincha, J. R. Frade, F. M. B. Marques, Protonic conduction in $La_2Zr_2O_7$-based pyrochlore materials, Solid State Ionics, 99 (1997) 33-40.

45. J. A. Labrincha, J. R. Frade, F. M. B. Marques, Defect structure of $SrZrO_3$, Solid State Ionics 61 (1993) 71-75.

46. J. A. Labrincha, J. R. Frade, F. M. B. Marques, Protonic and oxygen-ion conduction in $SrZrO_3$-based materials, J. Mater. Sci. 77 (1995) 2785-2792.

47. T. Yajima, H. Susuki, T. Yogo, H. Iwahara, Protonic conduction in $SrZrO_3$-based oxides, Solid State Ionics 51 (1992) 101-107.

48. H. Iwahara, H. Uchida, K. Ono, J. Ogaki, Proton conduction in sintered oxides based on $BaCeO_3$ J. Electrochem. Soc. 135 (1988) 529-533.

Table 1. Refined unit cell parameters, polymorph content and Rietveld agreement factors for $Sr_2Si_{1-x}Al_xO_{4-x/2}\square_{x/2}$ (x=0, 0.028, 0.06 and 0.075) series.

	Sr_2SiO_4	$Sr_2Si_{0.972}Al_{0.028}O_{3.986}$	$Sr_2Si_{0.94}Al_{0.06}O_{3.97}$	$Sr_2Si_{0.925}Al_{0.075}O_{3.9625}$
Monoclinic polymorph (M)				
a (Å)	5.6614(1)	5.6597(1)	5.6609(6)	5.6602(9)
b (Å)	7.0807(1)	7.0790(2)	7.0786(7)	7.0775(9)
c (Å)	9.7575(1)	9.7678(2)	9.7744(9)	9.7766(9)
β (º)	92.626(1)	92.532(2)	92.479(8)	92.511(9)
V/Z (Å^3)	97.68(1)	97.74(1)	97.83(5)	97.82(1)
Amount (wt%)	87.6(1)	23.7(1)	8.0(1)	7.8(2)
Orthorhombic polymorph (O)				
a (Å)	21.2295(8)	21.2227(2)	21.2213(2)	21.2231(2)
b (Å)	9.7417(3)	9.7526(1)	9.7560(1)	9.7572(1)

c (Å)	5.6685(2)	5.6691(1)	5.6698(1)	5.6697(1)
V (Å^3)	97.69(5)	97.78(2)	97.82(2)	97.84(1)
Amount (wt%)	12.4(1)	76.3(1)	92.0(1)	92.2(1)
R_{wp} (%)	11.08	11.55	12.91	14.07
R_p (%)	8.38	8.56	9.28	10.09
R_F^M/R_F^O	2.66/3.86	3.64/3.60	4.97/4.18	5.22/4.49

Table 2. Refined unit cell parameters, polymorph content and Rietveld agreement factors for $Sr_2Si_{0.94}Al_{0.06}O_{3.97}\square_{0.03}$ at different temperatures.

Temperature	**30 ºC**	**250 ºC**	**500 ºC**	**750 ºC**	**900 ºC**
V/Z (M/O)(Å^3)	97.94(5)/97.95(2)	98.77(3)	99.80(1)	100.97(1)	101.69(1)
Amount M/O (wt%)	8.0(1)/92.0(1)	100	100	100	100
R_{wp} (%)	14.25	15.25	13.46	14.45	14.65
R_p (%)	10.40	11.41	9.13	10.02	10.45
R_F^M/R_F^O	6.33/4.41	5.85	4.67	6.11	7.11

M = Monoclinic ($P12_1/n1$ space group)
O = Orthorhombic ($Pna2_1$ at T≤250 ºC and Pnma space groups)

Table 3. Conductivity values for $Sr_2Si_{1-x}Al_xO_{4-x/2}\square_{x/2}$ (x=0, 0.028, 0.06 and 0.075) series at 800 ºC in several flowing atmospheres: dry and wet N_2 and dry and wet O_2.

	Dry N_2 (S cm^{-1})	**Wet N_2 (S cm^{-1})**	**Dry O_2 (S cm^{-1})**	**Wet O_2 (S cm^{-1})**
Sr_2SiO_4	$1.5\ 10^{-6}$	$4.3\ 10^{-6}$	$1.2\ 10^{-5}$	$1.6\ 10^{-5}$
$Sr_2Si_{0.972}Al_{0.028}O_{3.986}$	$4.8\ 10^{-6}$	$5.3\ 10^{-6}$	$1.9\ 10^{-5}$	$2.1\ 10^{-5}$
$Sr_2Si_{0.94}Al_{0.06}O_{3.97}$	$5.1\ 10^{-6}$	$2.5\ 10^{-5}$	$1.3\ 10^{-5}$	$3.3\ 10^{-5}$
$Sr_2Si_{0.925}Al_{0.075}O_{3.9625}$	$2.4\ 10^{-6}$	$3.0\ 10^{-5}$	$3.8\ 10^{-5}$	$8.3\ 10^{-5}$

Figure captions

Figure 1. Crystal structure of Sr_2SiO_4, with the SiO_4 groups shown as tetrahedra and strontium 1 and strontium 2 cations displayed as spheres, respectively. (left) Projection close to the cb plane for the monoclinic polymorph. (right) Projection close to the cb plane for the orthorhombic polymorph ($Pna2_1$).

Figure 2. XRPD patterns for a) Sr_2SiO_4, b) $Sr_2Si_{0.972}Al_{0.028}O_{3.986}$, c) $Sr_2Si_{0.94}Al_{0.06}O_{3.97}$ and d) $Sr_2Si_{0.925}Al_{0.075}O_{3.9625}$ after firing at 1550 ºC.

Figure 3. Observed (crosses), calculated (full line) and difference (bottom) Rietveld refined XRPD patterns for $Sr_2Si_{0.94}Al_{0.06}O_{3.97}$. The vertical bars are the allowed Bragg reflections.

Figure 4. XRPD patterns from 30 to 900 ºC for $Sr_2Si_{0.94}Al_{0.06}O_{3.97}$ in the (left) 25-29 and 29-32 º2θ angular range. Monoclinic and orthorhombic $Pna2_1$ reflections are labelled as * and ▲, respectively.

Figure 5. TG curves, from the top to the bottom, for Sr_2SiO_4, $Sr_2Si_{0.972}Al_{0.028}O_{3.986}$, $Sr_2Si_{0.94}Al_{0.06}O_{3.97}$ and $Sr_2Si_{0.925}Al_{0.075}O_{3.9625}$ on cooling under humidified synthetic air and for $Sr_2Si_{0.925}Al_{0.075}O_{3.9625}$ on cooling under dry synthetic air.

Figure 6. SEM micrograph of polished and thermally etched surface of sintered pellets for a) Sr_2SiO_4, b) $Sr_2Si_{0.972}Al_{0.028}O_{3.986}$, c) $Sr_2Si_{0.94}Al_{0.06}O_{3.97}$ and d) $Sr_2Si_{0.925}Al_{0.075}O_{3.9625}$.

Figure 7. Complex impedance spectra at 800 ºC for $Sr_2Si_{0.94}Al_{0.06}O_{3.97}$ under several flowing atmospheres.

Figure 8. Arrhenius plots of log σ_T for (left) Sr_2SiO_4 and (right) $Sr_2Si_{0.94}Al_{0.06}O_{3.97}$ (same scale) under several flowing atmospheres and $Sr_{1.94}La_{0.06}SiO_{4.03}$ under a dry N_2 flow.

Figure 9. Overall conductivity data at 800 and 900 ºC as a function of oxygen partial pressure for $Sr_2Si_{0.94}Al_{0.06}O_{3.97}$. The inset shows the dependence of the ion oxide transference number, t_o, for the same sample under a dry 5%H_2–Ar/air gradient.

Table captions

Table 1. Refined unit cell parameters, polymorph content and Rietveld agreement factors for $Sr_2Si_{1-x}Al_xO_{4-x/2}\square_{x/2}$ (x=0, 0.028, 0.06 and 0.075) series.

Table 2. Refined unit cell parameters, polymorph content and Rietveld agreement factors for $Sr_2Si_{0.94}Al_{0.06}O_{3.97}\square_{0.03}$ at different temperatures.

Table 3. Conductivity values for $Sr_2Si_{1-x}Al_xO_{4-x/2}\square_{x/2}$ (x=0, 0.028, 0.06 and 0.075) series at 800 ºC in several flowing atmospheres: dry and wet N_2 and dry and wet O_2.

Figure

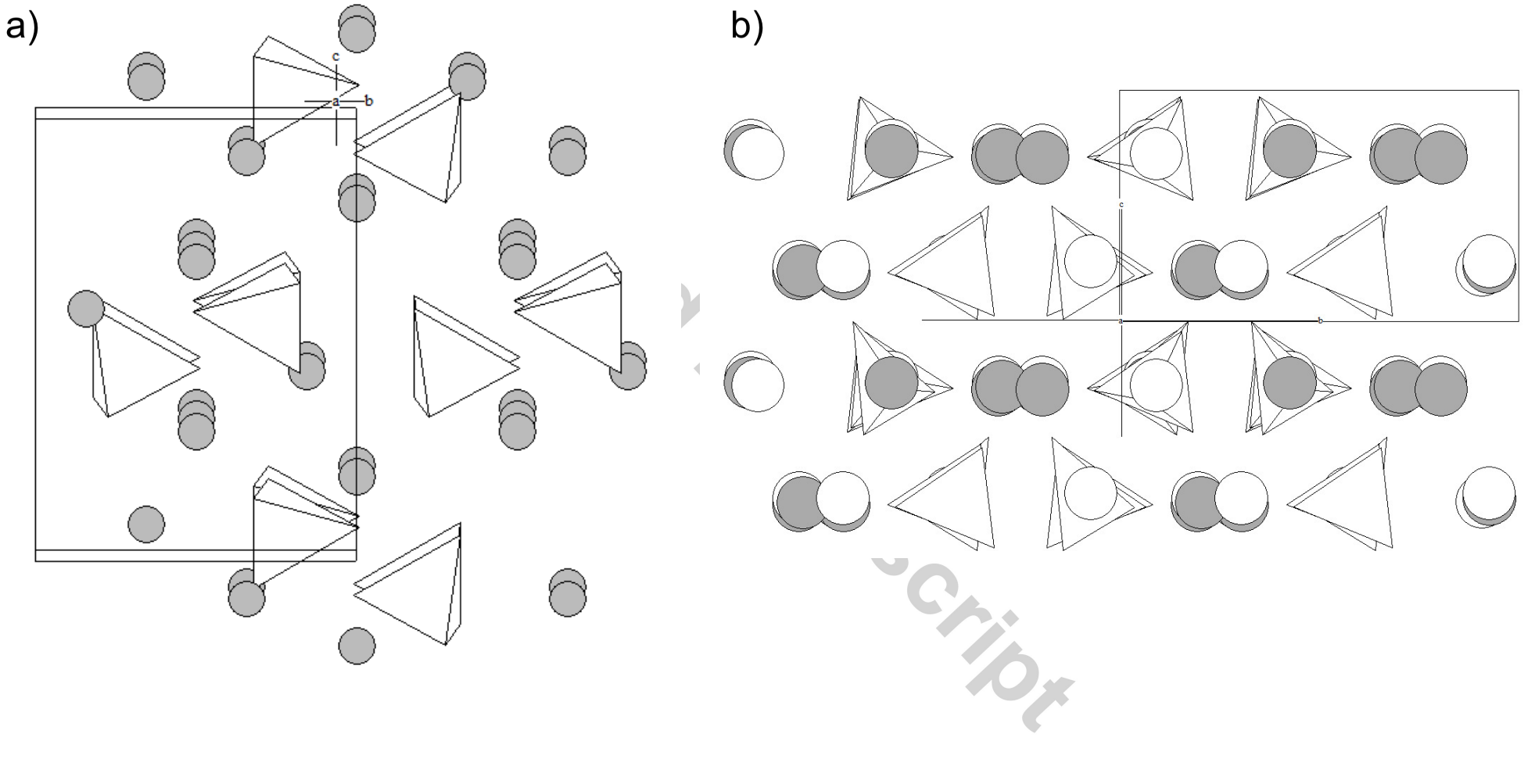

Figure 1

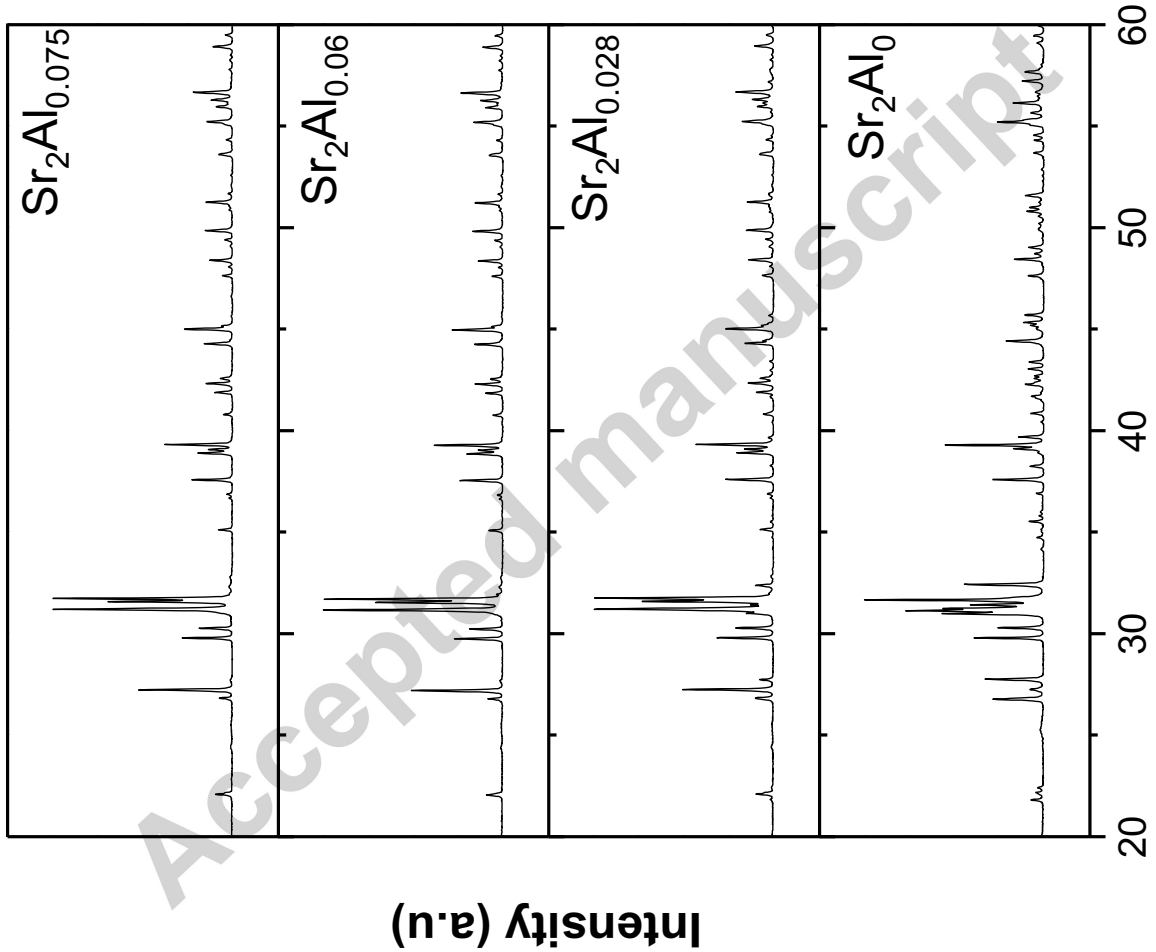

Figure 2

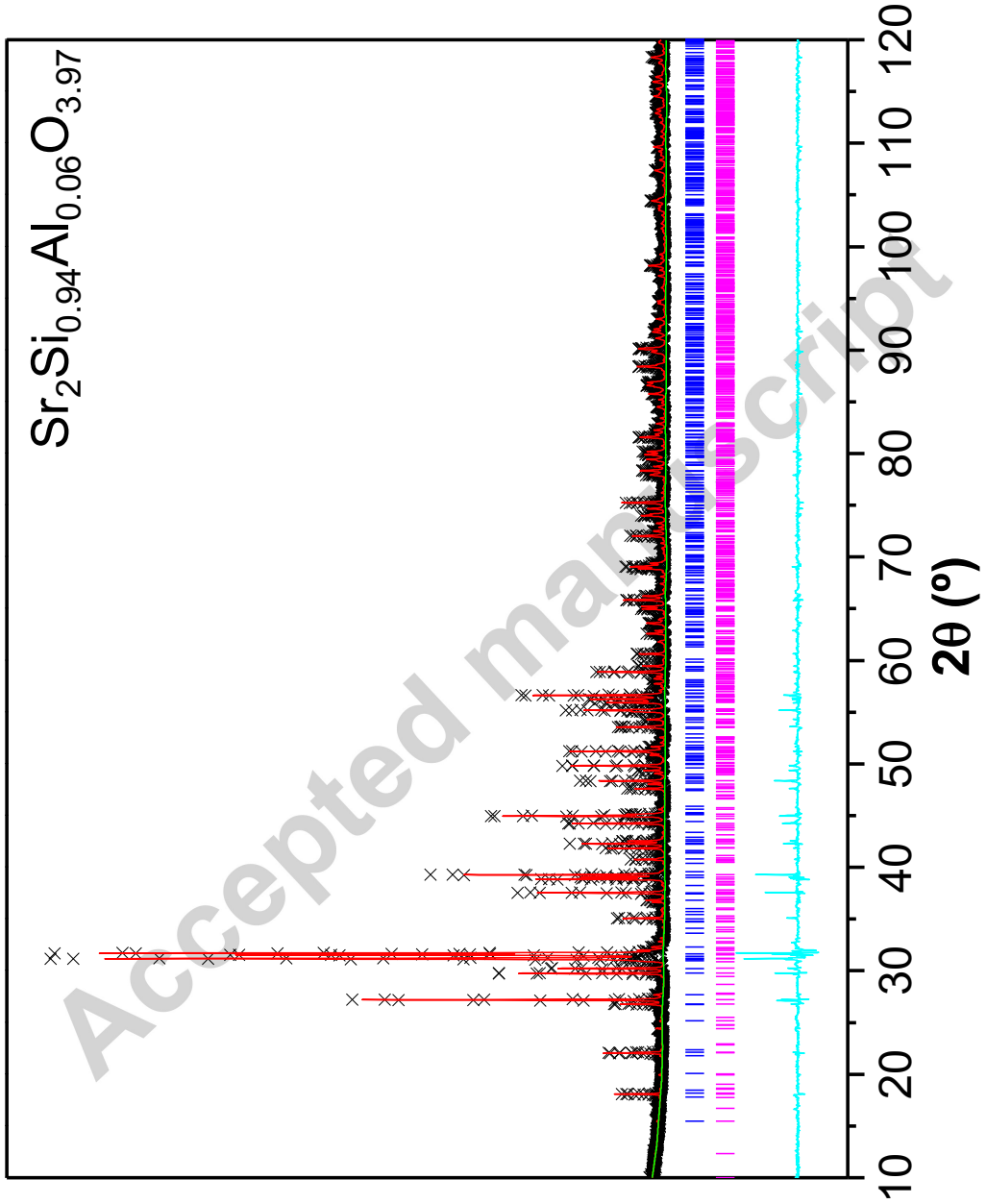

Figure 3

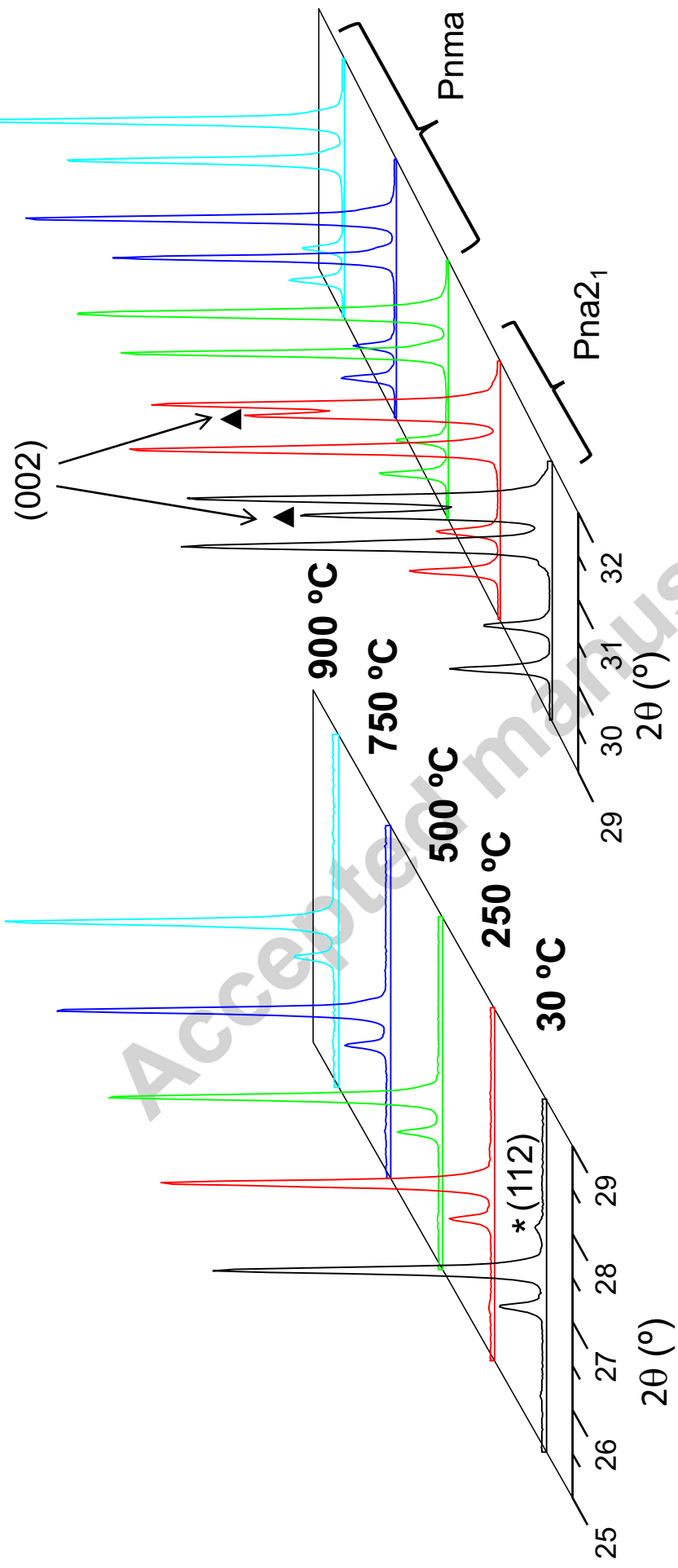

Figure 4

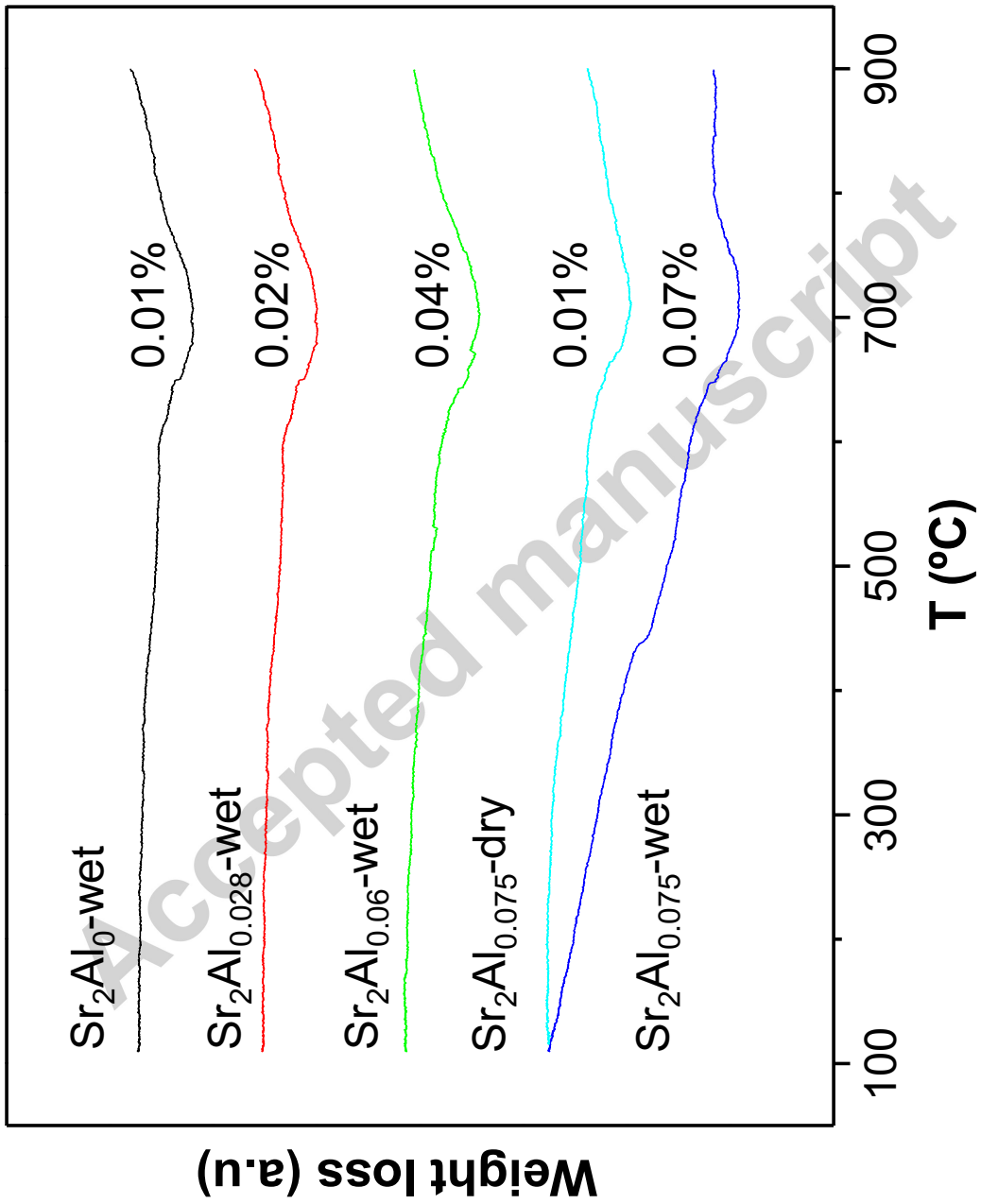

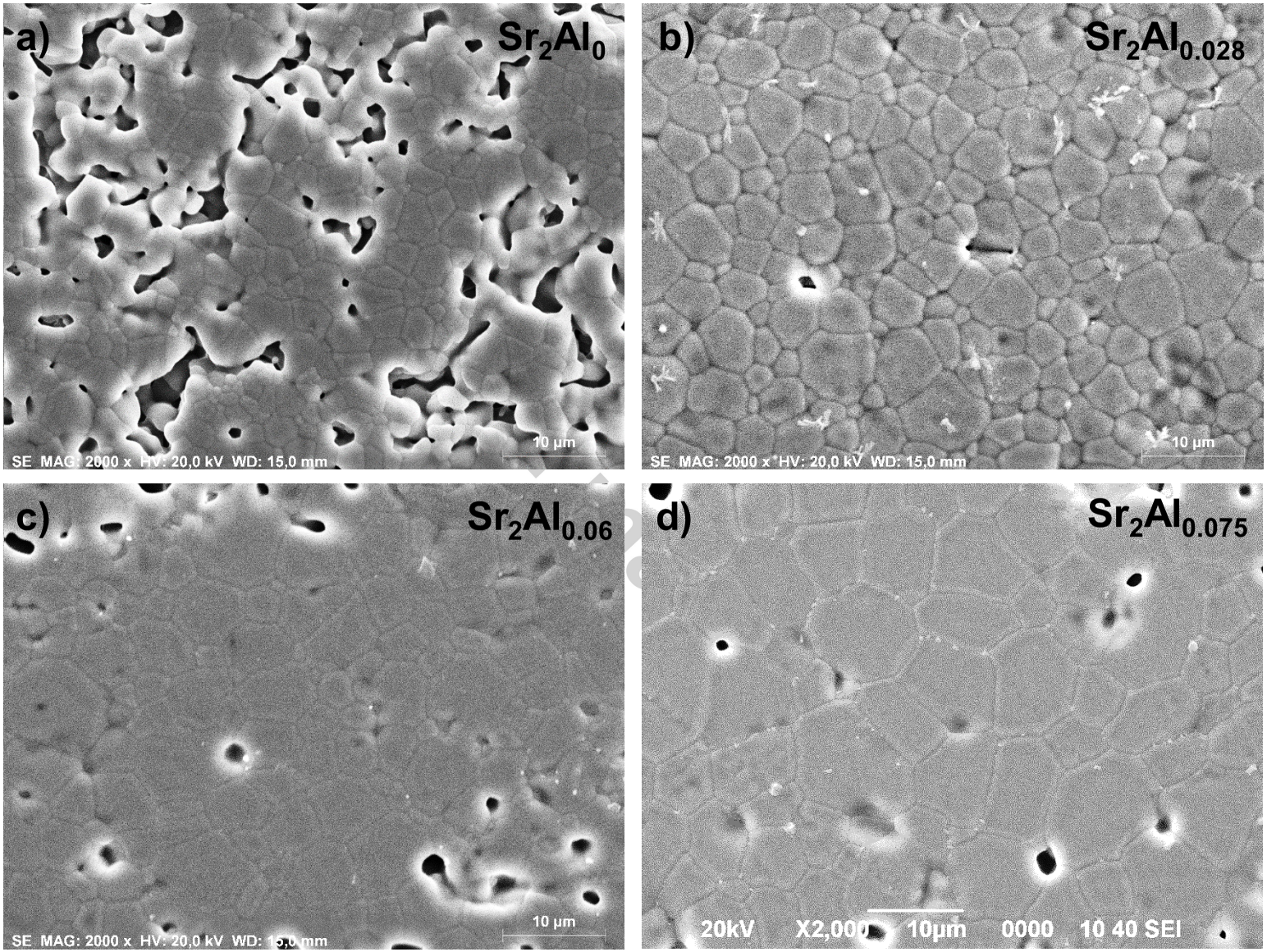

Figure 6

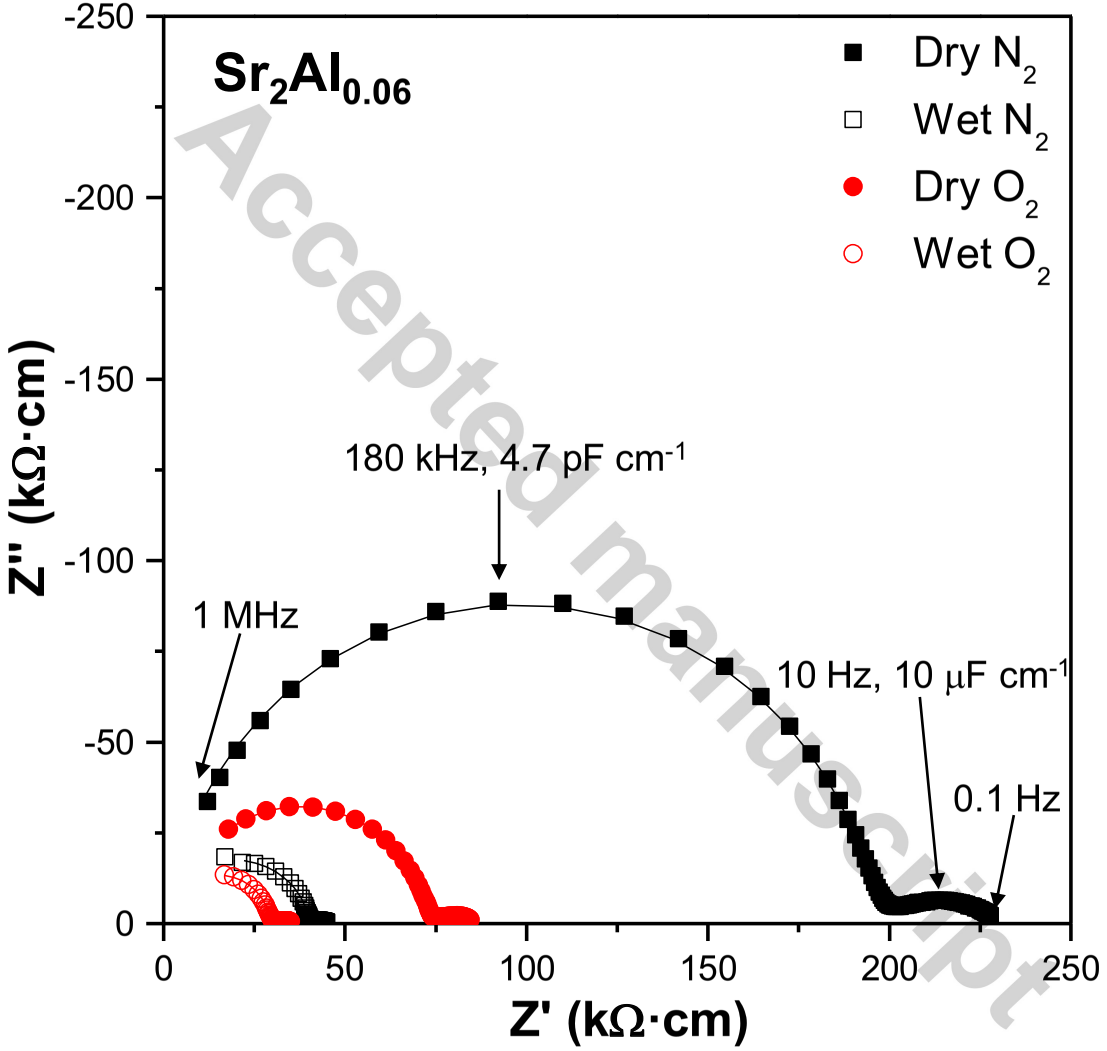

Figure 7

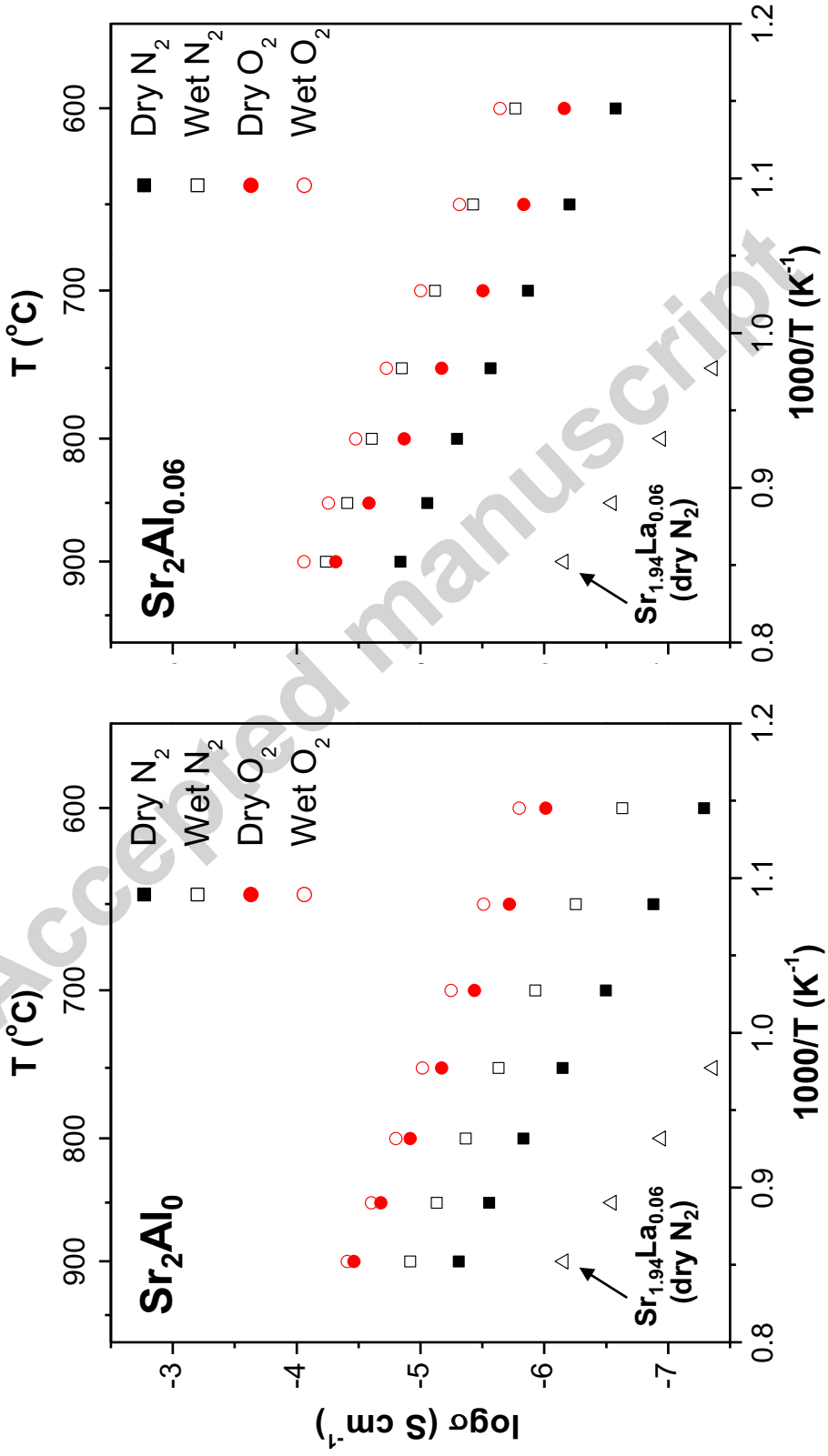

Figure 8

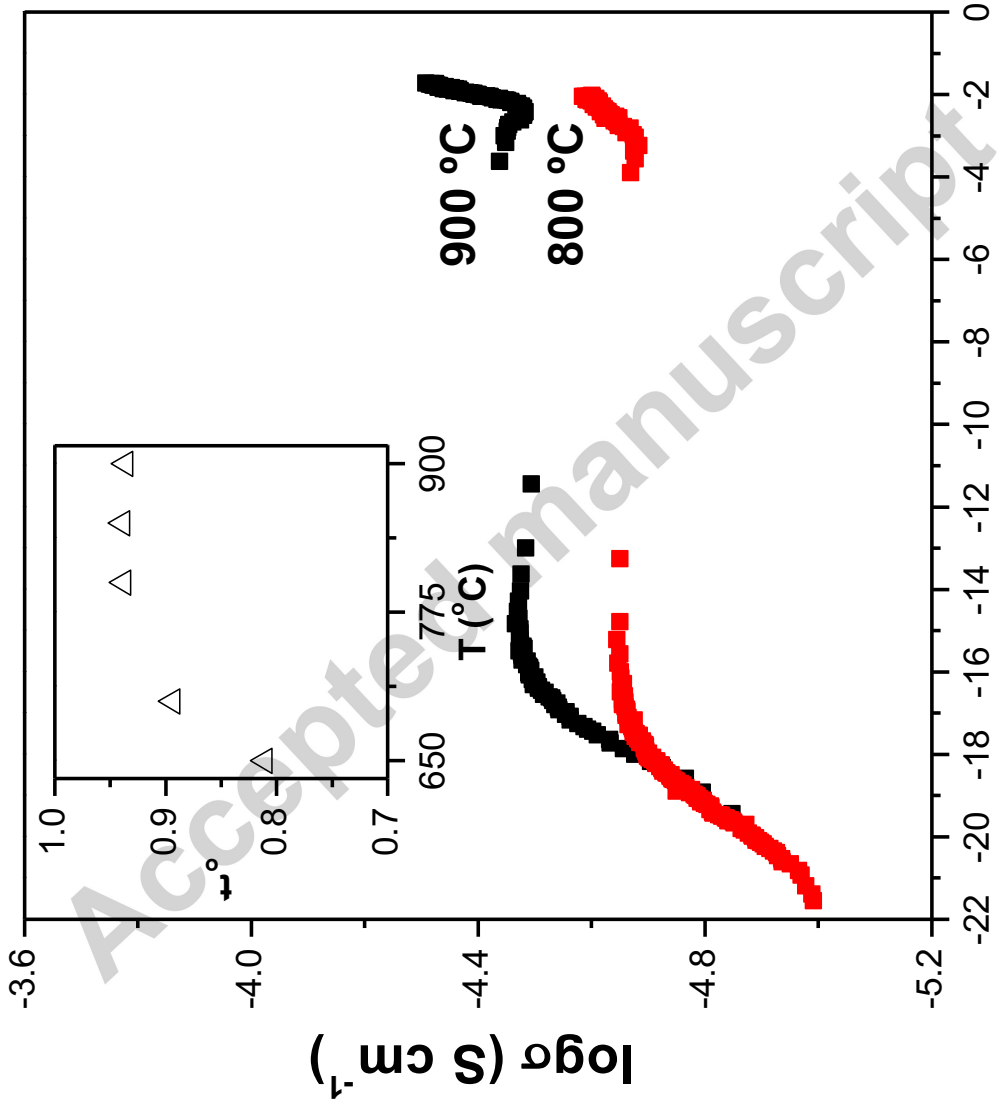

Figure 9